

Ab initio uncertainty quantification of neutrinoless double-beta decay in ^{76}Ge

A. Belley^{1,2,*}, J. M. Yao^{3,*}, B. Bally⁴, J. Pitcher^{1,2}, J. Engel⁵, H. Hergert^{6,7}, J. D. Holt^{1,8}, T. Miyagi^{9,10,17}, T. R. Rodríguez^{11,12,13}, A. M. Romero^{14,15}, S. R. Stroberg¹⁶, and X. Zhang³

¹TRIUMF, Vancouver, BC, Canada

²Department of Physics & Astronomy, University of British Columbia, Vancouver, BC, Canada

³School of Physics and Astronomy, Sun Yat-sen University, Zhuhai 519082, P.R. China.

⁴ESNT, IRFU, CEA, Université Paris-Saclay, 91191 Gif-sur-Yvette, France.

⁵Department of Physics and Astronomy, University of North Carolina, Chapel Hill, North Carolina 27516-3255, USA.

⁶Facility for Rare Isotope Beams, Michigan State University, East Lansing, Michigan 48824-1321, USA.

⁷Department of Physics & Astronomy, Michigan State University, East Lansing, Michigan 48824-1321, USA.

⁸Department of Physics, McGill University, Montréal, QC, Canada.

⁹Technische Universität Darmstadt, Department of Physics, 64289 Darmstadt, Germany.

¹⁰ExtreMe Matter Institute EMMI, GSI Helmholtzzentrum für Schwerionenforschung GmbH, 64291 Darmstadt, Germany.

¹¹Departamento de Estructura de la Materia, Física Térmica y Electrónica, Universidad Complutense de Madrid, E-28040 Madrid, Spain.

¹²Departamento de Física Teórica, Universidad Autónoma de Madrid, E-28049 Madrid, Spain.

¹³Centro de Investigación Avanzada en Física Fundamental-CIAFF-UAM, E-28049 Madrid, Spain.

¹⁴Departament de Física Quàntica i Astrofísica (FQA), Universitat de Barcelona (UB), c. Martí i Franqués, 1, 08028 Barcelona, Spain.

¹⁵Institut de Ciències del Cosmos (ICCUB), Universitat de Barcelona (UB), c. Martí i Franqués, 1, 08028 Barcelona, Spain.

¹⁶Department of Physics and Astronomy, University of Notre Dame, Notre Dame, IN 46556 USA.

¹⁷Max-Planck-Institut für Kernphysik, Saupfercheckweg 1, 69117 Heidelberg, Germany

*These authors contributed equally.

ABSTRACT

The observation of neutrinoless double-beta ($0\nu\beta\beta$) decay would offer proof of lepton number violation, demonstrating that neutrinos are Majorana particles, while also helping us understand why there is more matter than antimatter in the Universe. If the decay is driven by the exchange of the three known light neutrinos, a discovery would, in addition, link the observed decay rate to the neutrino mass scale through a theoretical quantity known as the nuclear matrix element (NME). Accurate values of the NMEs for all nuclei considered for use in $0\nu\beta\beta$ experiments are therefore crucial for designing and interpreting those experiments. Here, we report the first comprehensive ab initio uncertainty quantification of the $0\nu\beta\beta$ -decay NME, in the key nucleus ^{76}Ge . Our method employs nuclear strong and weak interactions derived within chiral effective field theory and recently developed many-body emulators. Our result, with a conservative treatment of uncertainty, is an NME of $3.44^{+1.33}_{-1.56}$, which, together with the best existing half-life sensitivity, sets an upper limit for effective neutrino mass of 141^{+117}_{-39} meV. The result is important for designing next-generation germanium detectors aiming to cover the entire inverted hierarchy region of neutrino masses. When extended to other isotopes, our approach will allow a careful comparison of experiments.

Introduction. The origin of the matter–antimatter asymmetry in the Universe remains one of the most important unsolved puzzles in physics. Many theories suggest that the asymmetry originates from a violation of lepton number through *leptogenesis*¹, in which leptons are created with no corresponding antileptons. The most promising way at present to determine the level at which lepton number is violated is through the hypothetical nuclear transition known as neutrinoless double-beta ($0\nu\beta\beta$) decay², in which two neutrons inside an atomic nucleus are transmuted into two protons, and two electrons are emitted without any of the antineutrinos that lepton-number

conservation requires. The detection of $0\nu\beta\beta$ decay would immediately demonstrate that neutrinos are Majorana fermions³, i.e., their own antiparticles, and therefore have significant implications for the Universe’s matter–antimatter asymmetry. Furthermore, if $0\nu\beta\beta$ decay is mediated by light Majorana neutrino exchange, its half-life can be related to an effective neutrino mass $\langle m_{\beta\beta} \rangle = \sum_i U_{ei}^2 m_i$, where m_i are the masses of light neutrinos, and U_{ei} are elements of the unitary matrix that mixes electron neutrinos with other flavors. The precision with which $\langle m_{\beta\beta} \rangle$ can be determined depends on how well the nuclear matrix element (NME) that governs the decay can be

calculated.

^{76}Ge is one of only a few highly promising candidate nuclei for experiments, as germanium detectors possess the advantages of high energy resolution, low internal background, and high detection efficiency. Several experiments have been searching for $0\nu\beta\beta$ decay in this isotope, including the GERDA⁴, Majorana Demonstrator (MJD)⁵, and CDEX⁶ collaborations. The highest half-life sensitivity so far has been reported by the GERDA experiment, which set a limit $T_{1/2} > 1.8 \times 10^{26}$ years at 90% confidence level (C.L.)⁴. If light-neutrino exchange is responsible, this half-life limit establishes an upper limit for the effective neutrino mass of $\langle m_{\beta\beta} \rangle = 73 - 204$ meV. The large range is due mainly to a spread of about a factor of three in the NMEs predicted by different nuclear models⁷⁻¹³. The spread can be even larger when the NMEs from all existing calculations with different parametrizations are considered. The associated uncertainty is difficult to reduce because each model has its particular phenomenological assumptions and uncontrolled approximations¹⁴⁻¹⁷.

In recent years, significant progress has been made in calculating NMEs from first principles. The required advances in *ab initio* nuclear theory have followed the parallel development of nuclear forces from chiral effective field theory (χ EFT)^{18,19}, a systematically improvable low-energy expansion of QCD, where undetermined low-energy constants (LECs) are optimized to data in few-nucleon systems, and similarity-renormalization-group (SRG) methods²⁰ for evolving such forces to the low-energy scale typical for atomic nuclei. With the resulting interactions and operators, the A -body Schrödinger equation can now be solved fairly accurately for most atomic nuclei in the medium-mass region²¹, and even in the ^{208}Pb region²², by employing nonperturbative and systematically improvable many-body methods. The application of *ab initio* methods to $0\nu\beta\beta$ decay is important because theoretical uncertainties related to the many-body wave functions and transition operators become controllable.

So far, three *ab initio* methods, the in-medium generator coordinate method (IM-GCM)²³, the valence-space formulation of the in-medium SRG (VS-IMSRG)²⁴, and coupled-cluster theory²⁵, have been used to calculate the NME of ^{48}Ca , the lightest nucleus that could be used in an experiment. When starting from the same chiral two-nucleon-plus-three-nucleon (NN+3N) interaction and $0\nu\beta\beta$ -decay operators, the approaches obtain results that agree within roughly estimated uncertainties. These methods were also successfully benchmarked against one another, as well as against quasi-exact diagonalization in light nuclei²⁵⁻²⁷. The difference between NMEs for $0\nu\beta\beta$ decay calculated with different *ab initio* methods but the same input has been found to give a useful approximation to the inaccuracies caused by truncation in many-body methods. These studies make it feasible to carry out uncertainty quantification in the *ab initio* prediction of the NMEs of experimentally relevant nuclei.

The second-lightest such nucleus, ^{76}Ge , is, along with ^{136}Xe , one of the two most important isotopes for experimen-

Table 1. The recommended value for the total NME of $0\nu\beta\beta$ decay in ^{76}Ge , together with the uncertainties from different sources.

$M^{0\nu}$	ϵ_{LEC}	$\epsilon_{\chi\text{EFT}}$	ϵ_{MBT}	ϵ_{OP}	ϵ_{EM}
$3.44^{+1.33}_{-1.56}$	0.9	0.3	0.8	0.5	<0.06

tal searches, and is now within the reach of multiple *ab initio* methods. The VS-IMSRG was the first *ab initio* approach to calculate the NME for ^{76}Ge , using the long-range (LR) transition operator associated with standard light-neutrino exchange²⁴. The resulting NME, 2.14(9), was 25-45% smaller than those obtained from phenomenological shell-model calculations. However, the contributions of the recently discovered leading-order short-range (SR) contact transition operator²⁸ and higher-order terms were not evaluated. In this work, we now include these contributions and present the first comprehensive uncertainty quantification for the NME in ^{76}Ge with two *ab initio* methods, using strong and weak interactions consistently derived within χ EFT.

Quantifying the uncertainty in the $0\nu\beta\beta$ -decay NME. For the $0\nu\beta\beta$ decay $^{76}\text{Ge}(0_1^+) \rightarrow ^{76}\text{Se}(0_1^+) + 2e^-$, the NME, called $M^{0\nu}$, can be written as:

$$M^{0\nu} = \langle ^{76}\text{Se}(0_1^+) | \hat{O}^{0\nu} | ^{76}\text{Ge}(0_1^+) \rangle, \quad (1)$$

where the decay operator $\hat{O}^{0\nu}$ is given in Methods. The main challenge in the assessment of theoretical error is the propagation of the uncertainties in the LECs from the chiral interaction through the complicated many-body calculations that ultimately produce the NME. To this end, we use the Sampling/Importance Resampling²⁹ formulation of Bayes' theorem for discrete samples, as was done in Ref.²² to obtain a theoretical uncertainty on the neutron skin of ^{208}Pb .

Following this procedure, a posterior predictive distribution (PPD) of the NMEs depending on the LECs (\mathbf{c}) is given by

$$\text{PPD} = \{M_k^{0\nu}(\mathbf{c}) : \mathbf{c} \sim \mathcal{P}(\mathbf{c}|\text{calibration})\}, \quad (2)$$

where $M_k^{0\nu}$ represents the NME from a specific theoretical calculation (i.e. using a particular many-body method and operators truncated at order k) and $\mathcal{P}(\mathbf{c}|\text{calibration})$ represents the probability of an LEC sample to yield results for a set of calibration observables that match experimental data. We label the standard deviation coming from this (non-Gaussian) distribution ϵ_{LEC} to make comparison with other sources of error easier. In this work we use the neutron-proton scattering phase shift in the 1S_0 partial wave at lab energy of 50 MeV as our calibration observable, since it has recently been discovered to correlate strongly with the NMEs (see Methods). The NMEs for the LEC samples are then evaluated using the recently developed Multi-output Multi-fidelity Deep Gaussian Process (MM-DGP) emulator for the VS-IMSRG, which allows us to within minutes predict the results of billions of

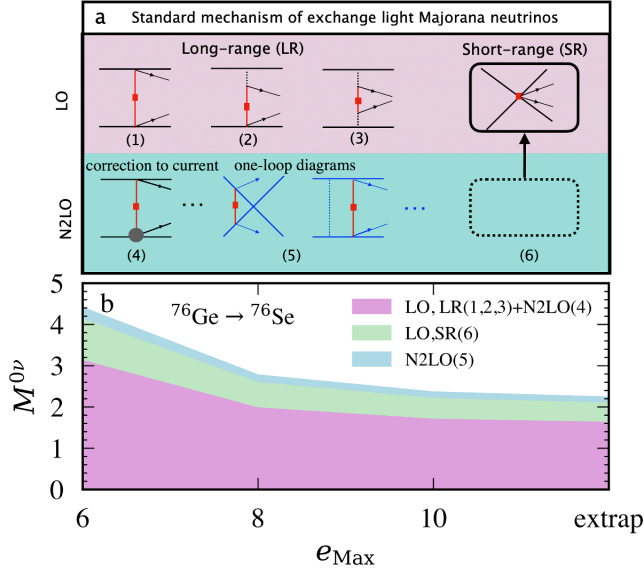


Figure 1. Hierarchy of contributions to $0\nu\beta\beta$ decay in chiral EFT, assuming light Majorana neutrino exchange. **a**, Diagrammatic contributions at different orders. **b**, The convergence of the NMEs for $^{76}\text{Ge} \rightarrow ^{76}\text{Se}$ using LO and N2LO transition operators. The red square indicates an insertion of LNV Majorana neutrino mass term $\langle m_{\beta\beta} \rangle$, and the gray circle represents corrections to the single-nucleon current parameterized in terms of form factors. The results are obtained from IM-GCM calculations using the EM1.8/2.0 interaction as a function of e_{Max} .

many-body calculations that would otherwise take years to perform in full.

We further assume that our errors are normally distributed and mutually independent, such that the true value of the NME in Eq. (1) can be written as:

$$M^{0\nu} = M_k^{0\nu} + \epsilon_{\chi\text{EFT}} + \epsilon_{\text{MBT}} + \epsilon_{\text{OP}} + \epsilon_{\text{EM}}, \quad (3)$$

where $\epsilon_{\chi\text{EFT}}$ represents the error coming from truncation of the nuclear forces, ϵ_{MBT} the error from the many-body method, ϵ_{OP} the error due to the truncation of the decay operator and finally, ϵ_{EM} the error on the emulated results. The values of the NME, together with the errors ϵ_i from different sources, are presented in Table 1. We detail below how each uncertainty is assessed.

We employ nuclear interactions derived in a formulation of χEFT where the Δ -isobars are considered explicitly³⁵. In particular, these interactions are given at next-to-next-to-leading order (N2LO) in the chiral expansion, where 17 LECs arise. These interactions are particularly useful for the present study since more diagrammatic contributions are considered at a given order in a Δ -full theory than in a Δ -less one, and the LECs come out more natural.

To assess $\epsilon_{\chi\text{EFT}}$, we need to estimate the contributions coming from neglected higher orders. We do so using a recently developed technique³⁶, where, by examining the order-

by-order NME convergence, we obtain a 68% degree of belief interval of 0.27 with the Δ -full interaction, upon which the interactions in this work are based³⁵. To be conservative, we choose $\epsilon_{\chi\text{EFT}}$ to be 0.3, as other parameterizations might have a slower rate of convergence. The results are shown in Extended Data Fig. 1, compared to the convergence of particular Δ -less nuclear interactions, available at NLO, N2LO, N3LO, and N4LO^{37,38}. As expected, we find more rapid convergence for the Δ -full interaction. Additionally, we observe the change from N3LO to N4LO to be much smaller, indicating that a future analysis with nuclear interactions at N3LO would allow us to greatly reduce that uncertainty.

To estimate ϵ_{MBT} , two *ab initio* methods, i.e., IM-GCM²³ and VS-IMSRG³⁹ (described in the Methods), are employed. These calculations are carried out using the NN+3N chiral interaction, denoted EM1.8/2.0⁴⁰, where the previous VS-IMSRG value²⁴ was found to be $M_{\text{LR}}^{0\nu} = 2.14(9)$. Here we also compute the contribution of the SR contact transition operator and find an overall $\sim 40\%$ increase in the NME to $M^{0\nu} = 2.94(8)$, with uncertainty coming from both the single-particle basis extrapolation to infinity as well as reference state dependence (see Methods). Similar calculations are carried out with the IM-GCM, yielding a long-range NME of $M_{\text{LR}}^{0\nu} = 1.67$ and total NME of $M^{0\nu} = 2.25(11)$, where the uncertainties are from the extension of model space with cranking configurations (Extended Data Table 1 and 2). In both approaches we find that the NMEs are significantly increased by the SR transition operator, confirming that it contributes at LO. On the other hand, the results show a modest deviation, where the VS-IMSRG NME is $\sim 30\%$ larger than that from the IM-GCM. We use the largest discrepancy of 0.83 as an estimate of ϵ_{MBT} . This difference is somewhat larger than what was found in ^{48}Ca ^{23,24}. This can be understood from the fact that the low-lying states in ^{48}Ca and ^{48}Ti are relatively simple and the quadrupole collectivity of ^{48}Ti is adequately captured in both methods. In contrast, the low-lying states of ^{76}Ge and ^{76}Se exhibit strong shape-coexistence and collectivity, including significant triaxiality^{41–43}. While these collective degrees of freedom are difficult to capture within the VS-IMSRG and other *ab initio* methods starting from spherical references^{44,45}, they are efficiently incorporated within the IM-GCM, as can be seen by comparing excitation spectra and electric multipole transitions with the experimental values (see Methods and Extended Data). We expect that future systematic improvements to the many-body truncations will improve the agreement between the two methods.

The errors from the $0\nu\beta\beta$ decay transition operators, collectively labeled ϵ_{OP} , can be separated into three sources: determination of the LEC of the SR transition operator, the use of the closure approximation, and the truncation of contributions beyond LO in the operator expansion. The two first uncertainties are the easiest to assess, as they have, respectively, been evaluated to be about 30% of the SR NME and 10% of the LR NME from phenomenological shell-model studies⁴⁶. For the third source, Fig. 1(a) presents the different

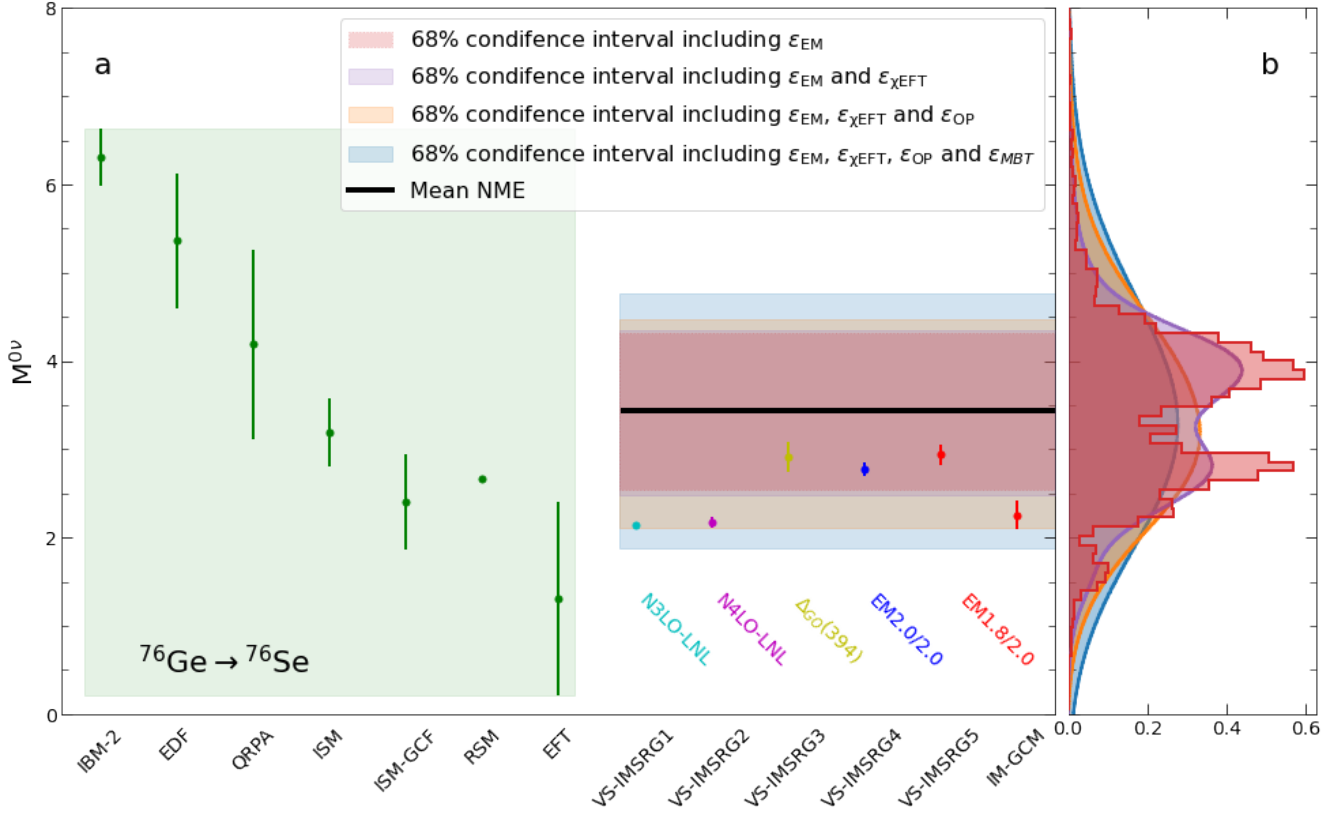


Figure 2. Comparison of $0\nu\beta\beta$ -decay NMEs in ^{76}Ge from nuclear models and ab initio calculations. **a**, The NMEs from phenomenological models, including the interacting-boson model (IBM-2)^{9,30}, energy-density-functional (EDF) methods^{8,11}, quasiparticle random-phase approximation (QRPA)^{12,31,32}, interacting shell model (ISM)^{7,10}, ISM with generalized contact formalism (ISM-GCF)³³, realistic shell model (RSM)¹³ and effective field theory (EFT)³⁴, are compared to the results of the VS-IMSRG and IM-GCM using different chiral interactions. The error bars of phenomenological nuclear models reflect the discrepancy of calculations from different groups. **b**, The posterior distribution function of the $0\nu\beta\beta$ NME using the MM-DGP emulator of the VS-IMSRG with 8188 non-implausible samples of chiral interactions from which the confidence intervals are extracted. The final distribution including all errors yields a value of $M^{0\nu\beta\beta} = 3.44^{+1.33}_{-1.56}$. The samples are weighted by phase-shifts in the 1S_0 partial wave and ground state energies of the parent and daughter nuclei. The uncertainties ϵ_i from EFT, many-body, operator and emulator are then added independently. See text for details.

contribution to the $0\nu\beta\beta$ -decay operators at LO and N2LO, noting that there is no contribution at NLO. We compute the contribution of the genuine N2LO transition operators, c.f. Fig. 1, which cannot be absorbed into the form factors, while excluding the contributions requiring intermediate states of odd-odd nucleus (see Methods). Figure 1(b) displays the convergence of the NMEs at LO and N2LO with respect to e_{Max} , the number of harmonic oscillator major shells in the basis, in the IM-GCM calculation (see Extended Data Table 1 and Extended Data Fig. 2 for details). The correction of transition operators at N2LO to the NME shows a weak dependence on the renormalization scale μ (Extended Data Fig. 3), and is found to be 0.079 at $\mu = 500$ MeV, consistent with previous findings⁴⁷. This confirms that the N2LO contributions are small, and the power counting works well for the transition operators. It also suggests that the common practice of taking LO transition operators supplemented with dipole form fac-

tors is a good approximation, once the contact term is properly considered. In short, we take a conservative value $\epsilon_{OP} = 0.55$ which includes 0.13 from the uncertainty of the LEC of the SR transition operator, 0.34 from the use of closure approximation, and 0.08 from the truncation on the chiral expansion of transition operators.

Finally, ϵ_{EM} is given by the MM-DGP emulator as it is based upon Gaussian Processes, which inherently come with a variance for each prediction. We obtain the final predictive posterior distribution by sampling the PPD 10^8 times and adding errors independently sampled from a normal distribution for each ϵ term. Fig. 2 shows the PPDs obtained with each error term discussed above, added separately. We find that $M^{0\nu} = 3.44^{+1.33}_{-1.56}$, where the uncertainty represents a 68% confidence interval. We compare the PPD to results of the VS-IMSRG and IM-GCM obtained with the EM1.8/2.0 nuclear interaction and VS-IMSRG with 4 other state-of-the-art chiral

NN+3N interactions (Extended Data Fig. 4), which all fall in our confidence interval. The PPD given strictly by the variation of the LECs is found to be bimodal, with the lowest mode showing a better agreement with the other chiral interactions. This suggests that some other quantity that correlates with the NME might eliminate the higher mode, if added to the calibration observables, and finding such an observable would allow us to significantly reduce the uncertainty of the NME. Our prediction is further compared to NMEs from various phenomenological nuclear models, which do not include the contribution of the contact transition operator, as it is hard to quantify due to the unknown LEC in such approaches⁴⁸.

Conclusions. In summary, we have presented the first comprehensive uncertainty quantification in *ab initio* calculations of NMEs for the $0\nu\beta\beta$ decay of ^{76}Ge using nuclear interactions derived from χEFT and recently developed many-body emulators based on the standard mechanism of exchanging light Majorana neutrinos with transition operators truncated up to the N2LO. We have demonstrated that the NME converges rapidly with the chiral expansion, both for the transition operators and for the strong interactions. Considering the errors from different choices of chiral interactions and many-body solvers, our recommended value for the NME is $3.44^{+1.33}_{-1.56}$ (68% C.L.), which sets the current upper limit for the effective neutrino mass $\langle m_{\beta\beta} \rangle = 141^{+117}_{-39}$ meV. While this uncertainty is sizable, a clear path to reduce it is now available by considering nuclear interactions that go to higher order in the chiral expansion, reducing many-body truncation errors and improving the likelihood function with a few more relevant observables to remove the bimodal form of the distribution. With our NME, the next-generation tonne-scale Germanium experiment with the ability to discover $0\nu\beta\beta$ decay up to 1.3×10^{28} years⁴⁹ will set the upper limit on effective neutrino mass $\langle m_{\beta\beta} \rangle = 17^{+14}_{-5}$ meV, which encompasses almost the entire range of allowed values of inverted neutrino mass hierarchy. This paper complements recent NME calculations in heavy systems⁵⁰, illustrating the power of *ab initio* methods to potentially deliver quantified uncertainties for all key isotopes of experimental interest.

References

1. Fukugita, M. & Yanagida, T. Baryogenesis Without Grand Unification. *Phys. Lett.* **B174**, 45–47 (1986).
2. Furry, W. H. On Transition Probabilities in Double Beta-Disintegration. *Phys. Rev.* **56**, 1184–1193 (1939).
3. Schechter, J. & Valle, J. W. F. Neutrinoless double- β decay in $\text{SU}(2) \times \text{U}(1)$ theories. *Phys. Rev. D* **25**, 2951–2954 (1982).
4. Agostini, M. *et al.* Final Results of GERDA on the Search for Neutrinoless Double- β Decay. *Phys. Rev. Lett.* **125**, 252502 (2020).
5. Arnquist, I. J. *et al.* Final result of the majorana demonstrator’s search for neutrinoless double- β decay in ^{76}Ge . *Phys. Rev. Lett.* **130**, 062501 (2023).
6. Zhang, B. T. *et al.* Searching for ^{76}Ge neutrinoless double beta decay with the CDEX-1B experiment (2023). [2305.00894](#).
7. Menéndez, J., Poves, A., Caurier, E. & Nowacki, F. Disassembling the nuclear matrix elements of the neutrinoless $\beta\beta$ decay. *Nucl. Phys. A* **818**, 139 – 151 (2009).
8. Rodríguez, T. R. & Martínez-Pinedo, G. Energy density functional study of nuclear matrix elements for neutrinoless $\beta\beta$ decay. *Phys. Rev. Lett.* **105**, 252503 (2010).
9. Barea, J., Kotila, J. & Iachello, F. $0\nu\beta\beta$ and $2\nu\beta\beta$ nuclear matrix elements in the interacting boson model with isospin restoration. *Phys. Rev. C* **91**, 034304 (2015).
10. Horoi, M. & Neacsu, A. Shell model predictions for ^{124}Sn double- β decay. *Phys. Rev. C* **93**, 024308 (2016).
11. Song, L. S., Yao, J. M., Ring, P. & Meng, J. Nuclear matrix element of neutrinoless double- β decay: Relativity and short-range correlations. *Phys. Rev. C* **95**, 024305 (2017).
12. Fang, D.-L., Faessler, A. & Šimkovic, F. $0\nu\beta\beta$ -decay nuclear matrix element for light and heavy neutrino mass mechanisms from deformed quasiparticle random-phase approximation calculations for ^{76}Ge , ^{82}Se , ^{130}Te , ^{136}Xe , and ^{150}Nd with isospin restoration. *Phys. Rev. C* **97**, 045503 (2018).
13. Coraggio, L., Gargano, A., Itaco, N., Mancino, R. & Nowacki, F. Calculation of the neutrinoless double- β decay matrix element within the realistic shell model. *Phys. Rev. C* **101**, 044315 (2020).
14. Engel, J. Uncertainties in nuclear matrix elements for neutrinoless double-beta decay. *Journal of Physics G: Nuclear and Particle Physics* **42**, 034017 (2015).
15. Engel, J. & Menéndez, J. Status and future of nuclear matrix elements for neutrinoless double-beta decay: a review. *Rep. Prog. Phys.* **80**, 046301 (2017).
16. Yao, J. M., Meng, J., Niu, Y. F. & Ring, P. Beyond-mean-field approaches for nuclear neutrinoless double beta decay in the standard mechanism. *Prog. Part. Nucl. Phys.* **126**, 103965 (2022).
17. Agostini, M., Benato, G., Detwiler, J. A., Menéndez, J. & Vissani, F. Toward the discovery of matter creation with neutrinoless $\beta\beta$ decay. *Rev. Mod. Phys.* **95**, 025002 (2023).
18. Epelbaum, E., Hammer, H.-W. & Meissner, U.-G. Modern theory of nuclear forces. *Rev. Mod. Phys.* **81**, 1773–1825 (2009).
19. Machleidt, R. & Entem, D. R. Chiral effective field theory and nuclear forces. *Phys. Rept.* **503**, 1–75 (2011).

20. Bogner, S., Furnstahl, R. & Schwenk, A. From low-momentum interactions to nuclear structure. *Prog. Part. Nucl. Phys.* **65**, 94 – 147 (2010).
21. Stroberg, S. R., Holt, J. D., Schwenk, A. & Simonis, J. Ab initio limits of atomic nuclei. *Phys. Rev. Lett.* **126**, 022501 (2021).
22. Hu, B. *et al.* Ab initio predictions link the neutron skin of ^{208}Pb to nuclear forces. *Nature Phys.* **18**, 1196–1200 (2022).
23. Yao, J. M. *et al.* Ab initio treatment of collective correlations and the neutrinoless double beta decay of ^{48}Ca . *Phys. Rev. Lett.* **124**, 232501 (2020).
24. Belley, A., Payne, C. G., Stroberg, S. R., Miyagi, T. & Holt, J. D. Ab initio neutrinoless double-beta decay matrix elements for ^{48}Ca , ^{76}Ge , and ^{82}Se . *Phys. Rev. Lett.* **126**, 042502 (2021).
25. Novario, S. *et al.* Coupled-cluster calculations of neutrinoless double- β decay in ^{48}Ca . *Phys. Rev. Lett.* **126**, 182502 (2021).
26. Basili, R. A. M. *et al.* Benchmark neutrinoless double- β decay matrix elements in a light nucleus. *Phys. Rev. C* **102**, 014302 (2020).
27. Yao, J. M. *et al.* Ab initio benchmarks of neutrinoless double- β decay in light nuclei with a chiral hamiltonian. *Phys. Rev. C* **103**, 014315 (2021).
28. Cirigliano, V. *et al.* New leading contribution to neutrinoless double- β decay. *Phys. Rev. Lett.* **120**, 202001 (2018).
29. Smith, A. F. M. & Gelfand, A. E. Bayesian Statistics without Tears: A Sampling-Resampling Perspective. *Source: The American Statistician* **46**, 84–88 (1992).
30. Deppisch, F. F., Graf, L., Iachello, F. & Kotila, J. Analysis of light neutrino exchange and short-range mechanisms in $0\nu\beta\beta$ decay. *Phys. Rev. D* **102**, 095016 (2020).
31. Mustonen, M. T. & Engel, J. Large-scale calculations of the double- β decay of ^{76}Ge , ^{130}Te , ^{136}Xe , and ^{150}Nd in the deformed self-consistent skyrme quasiparticle random-phase approximation. *Phys. Rev. C* **87**, 064302 (2013).
32. Hyvärinen, J. & Suhonen, J. Nuclear matrix elements for $0\nu\beta\beta$ decays with light or heavy majorana-neutrino exchange. *Phys. Rev. C* **91**, 024613 (2015).
33. Weiss, R., Soriano, P., Lovato, A., Menendez, J. & Wiringa, R. B. Neutrinoless double- β decay: Combining quantum monte carlo and the nuclear shell model with the generalized contact formalism. *Phys. Rev. C* **106**, 065501 (2022).
34. Brase, C., Menéndez, J., Coello Pérez, E. A. & Schwenk, A. Neutrinoless double- β decay from an effective field theory for heavy nuclei. *Phys. Rev. C* **106**, 034309 (2022).
35. Jiang, W. G. *et al.* Accurate bulk properties of nuclei from $A = 2$ to ∞ from potentials with Δ isobars. *Phys. Rev. C* **102**, 054301 (2020).
36. Melendez, J. A., Furnstahl, R. J., Phillips, D. R., Pratola, M. T. & Wesolowski, S. Quantifying correlated truncation errors in effective field theory. *Phys. Rev. C* **100**, 044001 (2019).
37. Entem, D. R., Machleidt, R. & Nosyk, Y. High-quality two-nucleon potentials up to fifth order of the chiral expansion. *Phys. Rev. C* **96**, 024004 (2017).
38. Kravvaris, K., Quinlan, K. R., Quaglioni, S., Wendt, K. A. & Navrátil, P. Quantifying uncertainties in neutron- α scattering with chiral nucleon-nucleon and three-nucleon forces. *Phys. Rev. C* **102**, 024616 (2020).
39. Stroberg, S. R., Hergert, H., Bogner, S. K. & Holt, J. D. Nonempirical interactions for the nuclear shell model: An update. *Annu. Rev. Nucl. Part. Sci.* **69**, 307–362 (2019).
40. Simonis, J., Stroberg, S. R., Hebeler, K., Holt, J. D. & Schwenk, A. Saturation with chiral interactions and consequences for finite nuclei. *Phys. Rev. C* **96**, 014303 (2017).
41. Ayangeakaa, A. D. *et al.* Triaxiality and the nature of low-energy excitations in ^{76}Ge . *Phys. Rev. C* **107**, 044314 (2023).
42. Henderson, J. *et al.* Triaxiality in selenium-76. *Phys. Rev. C* **99**, 054313 (2019).
43. Rodríguez, T. Role of triaxiality in ^{76}Ge and ^{76}Se nuclei studied with Gogny energy density functionals. *J. Phys. G* **44**, 034002 (2017).
44. Henderson, J. *et al.* Testing microscopically derived descriptions of nuclear collectivity: Coulomb excitation of ^{22}Mg . *Phys. Lett. B* **782**, 468 (2018).
45. Stroberg, S. R. *et al.* Systematics of E2 strength in the sd shell with the valence-space in-medium similarity renormalization group. *Phys. Rev. C* **105**, 034333 (2022).
46. Sen'kov, R. A. & Horoi, M. Neutrinoless double- β decay of ^{48}Ca in the shell model: Closure versus nonclosure approximation. *Phys. Rev. C* **88**, 064312 (2013).
47. Pastore, S. *et al.* Neutrinoless double- β decay matrix elements in light nuclei. *Phys. Rev. C* **97**, 014606 (2018).
48. Jokiniemi, L., Soriano, P. & Menéndez, J. Impact of the leading-order short-range nuclear matrix element on the neutrinoless double-beta decay of medium-mass and heavy nuclei. *Phys. Lett. B* **823**, 136720 (2021).
49. Abgrall, N. *et al.* The Large Enriched Germanium Experiment for Neutrinoless Double Beta Decay (LEGEND). *AIP Conf. Proc.* **1894**, 020027 (2021).
50. Belley, A., Miyagi, T., Stroberg, S. R. & Holt, J. D. Ab initio calculations of neutrinoless $\beta\beta$ decay refine neutrino mass limits (2023). [arXiv:2307.15156](https://arxiv.org/abs/2307.15156).

51. Hergert, H. In-medium similarity renormalization group for closed and open-shell nuclei. *Physica Scripta* **92**, 023002 (2016).
52. Hergert, H. *et al.* Nuclear structure from the in-medium similarity renormalization group. *Journal of Physics: Conference Series* **1041**, 012007 (2018).
53. Yao, J. M., Engel, J., Wang, L. J., Jiao, C. F. & Hergert, H. Generator-coordinate reference states for spectra and $0\nu\beta\beta$ decay in the in-medium similarity renormalization group. *Phys. Rev. C* **98**, 054311 (2018).
54. Hinohara, N. & Engel, J. Proton-neutron pairing amplitude as a generator coordinate for double- β decay. *Phys. Rev. C* **90**, 031301 (2014).
55. Jiao, C. F., Engel, J. & Holt, J. D. Neutrinoless double- β decay matrix elements in large shell-model spaces with the generator-coordinate method. *Phys. Rev. C* **96**, 054310 (2017).
56. Zhang, X. *et al.* Optimization of the generator coordinate method with machine-learning techniques for nuclear spectra and neutrinoless double- β decay: Ridge regression for nuclei with axial deformation. *Phys. Rev. C* **107**, 024304 (2023).
57. Romero, A. M., Yao, J. M., Bally, B., Rodríguez, T. R. & Engel, J. Application of an efficient generator-coordinate subspace-selection algorithm to neutrinoless double- β decay. *Phys. Rev. C* **104**, 054317 (2021).
58. Hill, D. L. & Wheeler, J. A. Nuclear constitution and the interpretation of fission phenomena. *Phys. Rev.* **89**, 1102–1145 (1953).
59. Griffin, J. J. & Wheeler, J. A. Collective motions in nuclei by the method of generator coordinates. *Phys. Rev.* **108**, 311–327 (1957).
60. Frosini, M. *et al.* Multi-reference many-body perturbation theory for nuclei - iii. ab initio calculations at second order in pgcm-pt. *Eur. Phys. J. A* **58**, 64 (2022).
61. Borrajo, M., Rodríguez, T. R. & Egido, J. L. Symmetry conserving configuration mixing method with cranked states. *Phys. Lett., B* **746**, 341 – 346 (2015).
62. Bally, B. & Bender, M. Projection on particle number and angular momentum: Example of triaxial bogoliubov quasiparticle states. *Phys. Rev. C* **103**, 024315 (2021).
63. Tsukiyama, K., Bogner, S. K. & Schwenk, A. In-medium similarity renormalization group for open-shell nuclei. *Phys. Rev. C* **85**, 061304 (2012).
64. Bogner, S. K. *et al.* Nonperturbative shell-model interactions from the in-medium similarity renormalization group. *Phys. Rev. Lett.* **113**, 142501 (2014).
65. Stroberg, S. R., Hergert, H., Holt, J. D., Bogner, S. K. & Schwenk, A. Ground and excited states of doubly open-shell nuclei from ab initio valence-space hamiltonians. *Phys. Rev. C* **93**, 051301 (2016).
66. Stroberg, S. R. *et al.* Nucleus-dependent valence-space approach to nuclear structure. *Phys. Rev. Lett.* **118**, 032502 (2017).
67. Pitcher, J. *et al.* In preparation.
68. Cutajar, K., Pullin, M., Damianou, A., Lawrence, N. & González, J. Deep gaussian processes for multi-fidelity modeling (2019).
69. Rasmussen, C. & Williams, C. *Gaussian Processes in Machine Learning.* (2004). MIT Press (2005).
70. Jiang, W. G., Forssén, C., Djärv, T. & Hagen, G. Emulating ab initio computations of infinite nucleonic matter (2022). [2212.13216](#).
71. Belley, A. *et al.* In preparation.
72. Ekström, A., Hagen, G., Morris, T. D., Papenbrock, T. & Schwartz, P. D. Δ isobars and nuclear saturation. *Phys. Rev. C* **97**, 024332 (2018).
73. Pérez, R. N., Amaro, J. E. & Arriola, E. R. Coarse-grained potential analysis of neutron-proton and proton-proton scattering below the pion production threshold. *Phys. Rev. C* **88**, 064002 (2013).
74. Cirigliano, V., Dekens, W., de Vries, J., Graesser, M. L. & Mereghetti, E. Neutrinoless double beta decay in chiral effective field theory: lepton number violation at dimension seven. *JHEP* **12**, 082 (2017).
75. Cirigliano, V., Dekens, W., Mereghetti, E. & Walker-Loud, A. Neutrinoless double- β decay in effective field theory: The light-majorana neutrino-exchange mechanism. *Phys. Rev. C* **97**, 065501 (2018).
76. Cirigliano, V. *et al.* New leading contribution to neutrinoless double- β decay. *Phys. Rev. Lett.* **120**, 202001 (2018).
77. Wirth, R., Yao, J. M. & Hergert, H. Ab initio calculation of the contact operator contribution in the standard mechanism for neutrinoless double beta decay. *Phys. Rev. Lett.* **127**, 242502 (2021).
78. Šimkovic, F., Pantis, G., Vergados, J. D. & Faessler, A. Additional nucleon current contributions to neutrinoless double β decay. *Phys. Rev. C* **60**, 055502 (1999).
79. Yao, J. M. *et al.* Ab initio studies of the double-gamow-teller transition and its correlation with neutrinoless double- β decay. *Phys. Rev. C* **106**, 014315 (2022).
80. Hebeler, K., Bogner, S. K., Furnstahl, R. J., Nogga, A. & Schwenk, A. Improved nuclear matter calculations from chiral low-momentum interactions. *Phys. Rev. C* **83**, 031301 (2011).

METHODS

The in-medium generator coordinate method (IM-GCM).

The IM-GCM is a combination of multi-reference (MR)-IMSRG^{51,52} and GCM^{23,53}. In this approach, we use Hartree-Fock-Bogoliubov (HFB) calculations with variation after particle-number projection to find the best quasiparticle vacua that include correlations due to nuclear pairing correlations and deformation. For ⁷⁶Ge and ⁷⁶Se, which both exhibit shape coexistence, a reference ensemble of prolate, spherical and oblate states in each nucleus is employed. It is defined by the density operator $\rho = \sum_{\alpha=I,F;k=1,N} c_{\alpha}^k |\Phi_{\alpha}^k\rangle \langle \Phi_{\alpha}^k|$, where the $|\Phi_{\alpha}^k\rangle$ are the symmetry-restored states with spin-parity $I^{\pi} = 0^+$, obtained by projecting the lowest-energy quasiparticle vacua in each nucleus onto good angular momentum as well as particle number, and $\sum_{\alpha=I,F;k=1,N} c_{\alpha}^k = 1$. Having fixed our reference ensemble, we normal order the Hamiltonian with respect to it and decouple it from all its number-conserving excitations by applying a unitary transformation $U(s) = e^{\Omega(s)}$, where the anti-Hermitian Magnus operator $\Omega(s)$ is determined by solving a system of MR-IMSRG flow equations. All the operators of interest are evolved by the same $U(s)$, and then used as inputs of the subsequent GCM calculation for nuclear low-lying states and the $0\nu\beta\beta$ -decay nuclear matrix elements. Nuclear wave functions are constructed as a linear combination of symmetry-restored quasi-particle vacua¹⁶,

$$|\Psi_{\alpha}^{NZI}\rangle = \sum_{K,\mathbf{q}} f_K^{I,\alpha}(\mathbf{q}) |\Phi^{NZI}(\mathbf{q})\rangle, \quad (4)$$

where α distinguishes states with the same angular momentum I , and the basis state is constructed as

$$|\Phi^{NZI}(\mathbf{q})\rangle = P^N P^Z P_{MK}^I |\Phi(\mathbf{q})\rangle. \quad (5)$$

where the label \mathbf{q} refers to the lattice location of the configuration in multi-dimensional collective coordinate space. The wave functions $|\Phi(\mathbf{q})\rangle$ of quasi-particle vacua are obtained from a constrained HFB calculation implemented with particle-number projection in the variation after projection scheme starting from the evolved Hamiltonian $\bar{H} = UH U^{\dagger}$.

The computational complexity of the IM-GCM increases significantly with the number of generator coordinates. In this work, we choose the three generator coordinates $(\beta, \gamma, \phi_{np})$ where (β, γ) are triaxial deformation parameters and ϕ_{np} is the neutron-proton isoscalar pairing amplitude $\phi_{np} = \langle \Phi(\mathbf{q}) | P_0^{\dagger} + P_0 | \Phi(\mathbf{q}) \rangle$. Here, we define the isoscalar pairing operator as^{54,55}

$$P_0^{\dagger} \equiv \frac{1}{\sqrt{2}} \sum_{\ell} \hat{\ell} [c_{\ell}^{\dagger} c_{\ell}^{\dagger}]_{000}^{L=0, J=1, T=0}, \quad (6)$$

where $\hat{\ell} \equiv \sqrt{2\ell+1}$, and L, J, T are the coupled orbital angular momentum, total angular momentum, and isospin of the pair (with the zero subscripts representing z projections). The number of total configurations is typically around $10^2 - 10^3$, posing a computational challenge for a general beyond mean-field calculation. The rotational symmetries in both gauge

and three-dimensional Euclidean space that are spontaneously broken in the basis configurations are restored via the particle number and angular momentum projector operators $P^{N,Z}$ and P_{MK}^I , respectively. Therefore, the complexity of IM-GCM calculations scales as $M_{\phi_n} M_{\phi_p} M_{\alpha} M_{\beta} M_{\gamma} (\sum_{d=1}^D N_d)^2$, where M refers to the number of mesh points in the rotation angles, D is the number of generator coordinates and N_d the number of mesh points along the d -th generator coordinate. To make this kind of study feasible, the IM-GCM calculation was optimized using a subspace reduction algorithm that employs machine-learning models as surrogates for exact quantum-number projection calculations for norm and Hamiltonian kernels⁵⁶. The subspace is determined using the energy transition-orthogonality procedure (ENTROP)⁵⁷.

The Extended Data Figure 8 displays the energies of states projected onto the particle numbers N, Z and angular momentum $I = 0$ for ⁷⁶Ge and ⁷⁶Se in the quadrupole deformation parameters (β, γ) plane from the IM-GCM calculation using the IMSRG-evolved chiral Hamiltonian of EM1.8/2.0. In contrast to the projected energy surface of ⁷⁶Ge with one pronounced triaxially deformed energy minimum, that of ⁷⁶Se is rather soft along the triaxiality parameter γ , which connects the oblate and prolate energy minima. The topology of the energy surfaces obtained with the EM1.8/2.0 and EM2.0/2.0 interactions is similar, indicating that it is not much sensitive to the SRG resolution of the nuclear interaction.

In Extended Data Figure 9, we show the variation of the NME with respect to the generator coordinates of the basis functions. The $0\nu\beta\beta$ decay is favored when the initial and final nuclear configurations have similar values of generator coordinates. This provides the foundation of the ENTROP algorithm⁵⁷ that is employed to optimize the IM-GCM calculation. Finally, the mixing coefficient for each basis function is determined from the variational principle which leads to the Hill-Wheeler-Griffin equation^{58,59}.

The energy spectra and reduced matrix elements of electric quadrupole transitions of the low-lying states of ⁷⁶Ge and ⁷⁶Se from the IM-GCM calculation are presented in Extended Data Table 3 and Extended Data Fig. 7. The main features of the ground-state and γ bands in ⁷⁶Ge are reproduced (better than in ⁷⁶Se), even though the spectra of both nuclei are overall stretched by a factor of 1.4 – 1.7. This spreading of the excitation spectrum seems to be a common feature of calculations using IMSRG-evolved Hamiltonians⁶⁰ as seen, for example, in ⁴⁸Ti²³. The possible reasons are as follows. In the IMSRG evolution, the excited states tend to gain less energy than that of ground state because the transformation is tuned for the latter. The reduced matrix elements are also reasonably reproduced, except that the low-lying states of ⁷⁶Se are slightly more weighted by the oblate deformed configurations, as expected from the location of global energy minimum shown in Extended Data Fig. 8. As a result, the $3_1^+, 5_1^+$ states of ⁷⁶Se are shifted to relatively high energies, as shown in the Extended Data Fig. 7.

Motivated by recent studies based on energy density func-

tionals^{61,62}, we have explored the inclusion of cranked configurations in (4) as a possible solution to the stretching of the spectrum. These configurations break time-reversal invariance, but the symmetry is restored when we project on good angular momentum. The Extended Data Fig. 7 shows that we can achieve some compression of the energy spectra of low-lying states, to a factor of about 1.3 – 1.6. At the same time, the NME for $0\nu\beta\beta$ decay is enhanced by about 10% (see Extended Data Table 2).

The valence-space in-medium similarity renormalization group (VS-IMSRG) and its emulator. In the VS-IMSRG, a continuous unitary transformation $U(s)$ is used to evolve a given normal-ordered chiral Hamiltonian to decouple the off-diagonal elements of the Hamiltonian that are connecting the P valence space and the excluded Q spaces^{39,63–66}. This procedure is realized by solving a flow equation with a properly chosen generator. As the flow parameter increases up to a sufficient large value, an effective Hamiltonian in the P valence space is obtained. To this end, we split the single-particle model space into core (c), valence particle (v) and nonvalence particle (q) orbitals. The actual shell model calculation for a nucleus with A nucleons is an exact diagonalization of the Hamiltonian matrix in a subspace of the Hilbert space that is spanned by configurations of the form

$$|v_1 \dots v_{A_v}\rangle \equiv a_{v_1}^\dagger \dots a_{v_{A_v}}^\dagger |\Phi_{A_c}\rangle, \quad (7)$$

where $|\Phi_{A_c}\rangle$ is the wavefunction for a suitable core with A_c nucleons, and the A_v valence nucleons are distributed over the valence orbitals v_i in all allowed ways. The matrix representation of the Hamiltonian in the space spanned by these configurations is

$$\langle v'_1 \dots v'_{A_v} | H | v_1 \dots v_{A_v} \rangle = \langle \Phi_{A_c} | a_{v'_1} \dots a_{v'_{A_v}}^\dagger H a_{v_1}^\dagger \dots a_{v_{A_v}}^\dagger | \Phi_{A_c} \rangle. \quad (8)$$

Previous studies^{39,66} have shown that using the core wavefunction $|\Phi_{A_c}\rangle$ as a reference state for normal ordering neglects important contributions from the valence-space 3N interaction. This issue is remedied by using an ensemble of Slater determinants with the mass number expectation value set to the mass number A of the target nucleus. We obtain the reference ensemble by solving the HF equations for the target nucleus in the equal-filling approximation where occupation numbers of m -substates of partially filled orbitals are set to equal values between 0 and 1. The irreducible density matrices of this ensemble vanish by construction^{39,66}. We note that in the case of neutrinoless double-beta decay, both the parent or daughter nuclei can be taken for the reference ensemble, as the many-body truncation will introduce some dependency on the reference. We therefore compare results using both reference ensembles to assess some of the effects of the many-body truncation. All the operators including the $0\nu\beta\beta$ -decay operators are evolved with the same unitary operator.

The multi-output multi-fidelity deep Gaussian process (MM-DGP) emulator⁶⁷ for the VS-IMSRG has recently been

developed to allow for the rapid prediction of results from many-body calculations without needing to carry out expensive calculations. Following the work from⁶⁸, it uses deep Gaussian Processes in which the results of a Gaussian Process⁶⁹ are fed to another as inputs sequentially to model multi-fidelity data. In this case, the different fidelity levels are taken to be calculations at $e_{\text{Max}} = 4$ (low-fidelity), 6, 8, 10, and 12 (high-fidelity). The MM-DGP builds upon this idea by adding a multi-output kernel to allow modeling of multiple outputs at the same time. By using this kind of architecture, the amount of data required to train the model can be significantly reduced, thereby reducing the number of costly high-fidelity training points required to optimize the emulator. In particular, we use 300, 100, 100, 50, and 50 points at each fidelity level, respectively, 10% of which is kept as validation data.

As show in Extended Data Figure 10, we obtain a very good agreement between the emulated NME results and the full VS-IMSRG calculations, with a coefficient of correlation of 0.995 between the two and a root-mean-square (rms) error of 0.13 on the validation data. Similar results are found for the ground state energies with a correlation coefficient of 0.996 and a rms error of 0.145 MeV in average binding energy. In both cases, the expected variance of the model well covers the the rms error, showing that a reasonable uncertainty is assigned to each prediction.

To construct the predictive posterior distribution of the NMEs, we consider 8188 non-implausible samples of the LECs obtained using history matching⁷⁰ for nuclear interactions in chiral EFT with explicit delta excitation degree of freedom at N2LO. At this order, 17 LECs are required. From the emulated NMEs obtained using these samples, we can construct posterior predictive distribution using the principle of sampling-importance resampling²⁹, an application of Bayes' theorem for discrete samples. Assuming a uniform prior between the different LECs samples \mathbf{c} (i.e. no sample is more likely than the others a priori), we assign a weight to each of them via a likelihood function $\mathcal{P}(\mathbf{c}|\text{calibration})$ representing how well the sample performs for a set of calibration observables. In our case, we use a normal distribution as our likelihood function with the prediction of neutron-proton phase shift in the 1S_0 partial wave at 50 MeV as our calibration observable, because it has been found to be correlated with the NMEs⁷¹. The variance of the calibration observable is dominated by the χEFT error, as shown in Ref.⁷² with the mean taken from the Granada phase shift analysis⁷³. We further compare our results with those using a student-t distribution for the likelihood and find the final results to agree within 1%. We therefore only consider the normal distribution likelihood.

The transition operators of $0\nu\beta\beta$ decay. Chiral EFT provides a systematical and consistent framework to derive transition operators of $0\nu\beta\beta$ decay and nuclear forces. Their contributions can be arranged into different orders based on the chiral power counting⁷⁴. Here, we only consider the transition operators for the standard mechanism, which have been

discussed in detail previously⁷⁵. The leading-order (LO) transition operators are described by tree-level neutrino exchange, see Fig. 1 of main text. The contribution of high-momentum neutrino exchange is included by introducing a short-range operator which has recently been proposed to be promoted to LO to ensure renormalizability⁷⁶. Thus, the transition operators at LO are given by

$$O_{\text{LO}}^{0\nu} = O_{\text{LO,LR}}^{0\nu} + O_{\text{LO,SR}}^{0\nu}, \quad (9)$$

where the long-range (LR) operator term can be divided into Fermi (F), Gamow-Teller (GT) and tensor (T) terms

$$O_{\text{LO,LR}}^{0\nu} = \tau_1^+ \tau_2^+ \left(O_{\text{F},0}^{\text{LO}} + O_{\text{GT},0}^{\text{LO}} \boldsymbol{\sigma}_1 \cdot \boldsymbol{\sigma}_2 + O_{\text{T},2}^{\text{LO}} S_{12}^r \right) \quad (10)$$

with $S_{12}^r \equiv 3(\boldsymbol{\sigma}_1 \cdot \hat{\mathbf{r}}_{12})(\boldsymbol{\sigma}_2 \cdot \hat{\mathbf{r}}_{12}) - \boldsymbol{\sigma}_1 \cdot \boldsymbol{\sigma}_2$, and $\hat{\mathbf{r}}_{12} = (\mathbf{r}_1 - \mathbf{r}_2)/|\mathbf{r}_1 - \mathbf{r}_2|$. The neutrino potentials $O_{\alpha,L}^{\text{LO}}$ are given by

$$O_{\alpha,L}^{\text{LO}}(r_{12}) = \frac{2R}{\pi g_A^2(0)} \int_0^\infty dq q^2 \frac{h_{\alpha,L}^{\text{LO}}(\mathbf{q}^2)}{q(q+E_d)} j_L(qr_{12}), \quad (11)$$

where α stands for F, GT, or T, respectively. The function $j_L(qr_{12})$ is the spherical Bessel function of rank L , where $L = 0$ for the Fermi and GT terms, and $L = 2$ for the tensor term. Furthermore,

$$h_{\text{F},0}^{\text{LO}}(\mathbf{q}^2) = -g_V^2(0), \quad (12a)$$

$$h_{\text{GT},0}^{\text{LO}}(\mathbf{q}^2) = g_A^2(0) - \frac{2}{3} \frac{\mathbf{q}^2}{2m_p} g_A(0) g_P(0) + \frac{1}{3} \frac{\mathbf{q}^4}{4m_p^2} g_P^2(0), \quad (12b)$$

$$h_{\text{T},2}^{\text{LO}}(\mathbf{q}^2) = \frac{2}{3} \frac{\mathbf{q}^2}{2m_p} g_A(0) g_P(0) - \frac{1}{3} \frac{\mathbf{q}^4}{4m_p^2} g_P^2(0). \quad (12c)$$

where the vector and axial-vector coupling constants are $g_V(0) = 1$, $g_A(0) = 1.27$. The pseudoscalar coupling $g_P(0) = g_A(0)2m_p/(\mathbf{q}^2 + m_\pi^2)$ has a momentum-dependence from the pion propagator.

The LO short-range (SR) operator is regularized with a non-local regulator⁷⁷,

$$O_{\text{LO,SR}}^{0\nu} = -2g_v^{NN} \left(\frac{m_N g_A^2}{4f_\pi^2} \right) f_\Lambda^{n_{\text{exp}}}(r_{12}) f_\Lambda^{n_{\text{exp}}}(r'_{12}) \quad (13)$$

where we adopt the following separable form

$$f_\Lambda^{n_{\text{exp}}}(r_{12}) = \frac{1}{2\pi^2} \int_0^\infty dq q^2 \exp\left[-\left(\frac{q}{\Lambda}\right)^{2n_{\text{exp}}}\right] j_0(qr_{12}). \quad (14)$$

Here the pion decay constant $f_\pi = 92.2 \text{ MeV}$. The momentum cutoff Λ and n_{exp} are parameters of the regulator whose values are chosen to be consistent with those of chiral nuclear forces. The LEC g_v^{NN} has been determined with different sets of chiral forces from the $nn \rightarrow ppe^-e^-$ process⁷⁷.

At the next-to-next-to-leading order (N2LO), part of the contribution can be absorbed into corrections to the single-nucleon currents, which are often included via momentum-dependent form factors⁷⁴

$$g_V(\mathbf{q}^2) = g_V(0) \left(1 + \mathbf{q}^2/\Lambda_V^2\right)^{-2}, \quad (15a)$$

$$g_A(\mathbf{q}^2) = g_A(0) \left(1 + \mathbf{q}^2/\Lambda_A^2\right)^{-2}. \quad (15b)$$

The cutoff values are $\Lambda_V = 0.85 \text{ GeV}$ and $\Lambda_A = 1.09 \text{ GeV}$ ^{78,79}. Contributions from the induced weak-magnetism (MM) terms to both GT and tensor parts of the NME also appear at N2LO, and they are given by

$$h_{\text{GT},0}^{\text{N2LO}}(\mathbf{q}^2) = g_M^2(\mathbf{q}^2) \frac{1}{6} \frac{\mathbf{q}^2}{m_p^2}, \quad (16a)$$

$$h_{\text{T},2}^{\text{N2LO}}(\mathbf{q}^2) = g_M^2(\mathbf{q}^2) \frac{1}{12} \frac{\mathbf{q}^2}{m_p^2}, \quad (16b)$$

where the form factor $g_M(\mathbf{q}^2) = g_V(\mathbf{q}^2)(1 + \kappa_1)$ is usually adopted with the anomalous nucleon iso-vector magnetic moment $\kappa_1 = \mu_n^{(a)} - \mu_p^{(a)} = 3.7$. We note that the frequently employed transition operators^{16,78} contain the contributions of the previous LO (12a-12c) and the N2LO (15a), (15b), and (16a), (16b) terms. The inclusion of these corrections regularizes the short-range contribution⁷⁹, quenching the NME of the LO operators.

There are additional N2LO contributions from one-loop diagrams which cannot be included via the form factors. The expressions for these non-factorizable contributions in momentum-space are derived in Ref.⁷⁵. Here we derive these transition operators in coordinate space. We have

$$O_{\text{N2LO}}^{0\nu} = \tau_1^+ \tau_2^+ \left(O_{\text{N2LO,GT}}^{0\nu} + O_{\text{N2LO,F}}^{0\nu} + O_{\text{N2LO,T}}^{0\nu} \right) \quad (17)$$

which is also decomposed into the GT, Fermi and tensor terms,

$$O_{\text{N2LO,GT}}^{0\nu} = \frac{4R}{3\pi m_\pi^2 T^2} \int q^4 dq j_0(qr) \left(K_{VV}(\tilde{q}) - K_{AA}(\tilde{q}) - \frac{2g_A^2 m_\pi^2}{q^2 + m_\pi^2} \ln \frac{m_\pi^2}{\mu_{us}^2} - K_{CT}(\tilde{q}) \right) \boldsymbol{\sigma}_1 \cdot \boldsymbol{\sigma}_2, \quad (18)$$

$$O_{\text{N2LO,F}}^{0\nu} = \frac{4R}{\pi T^2} \int q^2 dq j_0(qr) \left(\left[\frac{3C_T T^2}{\pi^2} - \frac{2g_A^2 q^2}{q^2 + m_\pi^2} \right] \ln \frac{m_\pi^2}{\mu_{us}^2} - K'_{AA}(\tilde{q}) + 2 \frac{g_v^{NN}}{g_A^2} \right) \mathbf{1}_1 \times \mathbf{1}_2, \quad (19)$$

$$O_{\text{N2LO,T}}^{0\nu} = \frac{4R}{3m_\pi^2 \pi T^2} \int q^4 dq j_2(qr) \left(K_{VV}(\tilde{q}) - K_{AA}(\tilde{q}) - \frac{2g_A^2 m_\pi^2}{q^2 + m_\pi^2} \ln \frac{m_\pi^2}{\mu_{us}^2} - K_{CT}(\tilde{q}) \right) S_{12}^r(\hat{r}), \quad (20)$$

with $\tilde{q} = q^2/m_\pi^2$, $T = 4\pi f_\pi$, and

$$K_{VV}(\tilde{q}) = \frac{2(1-\tilde{q})^2}{\tilde{q}^2(1+\tilde{q})} \ln(1+\tilde{q}) - \frac{2}{\tilde{q}} + \frac{7-3\tilde{q}L_\pi}{(1+\tilde{q})^2} + \frac{L_\pi}{1+\tilde{q}}, \quad (21)$$

$$K_{AA}(\tilde{q}) = \frac{g_A^2}{1+\tilde{q}}(L_\pi-4) + \frac{1}{(1+\tilde{q})^2}, \quad (22)$$

$$K'_{AA}(\tilde{q}) = -\frac{3}{4}(1-g_A)^2 L_\pi + g_A^4 f_4(\tilde{q}) + g_A^2 f_2(\tilde{q}) + f_0(\tilde{q}) + 24g_A^2 f_\pi^2 C_T (L_\pi + 1), \quad (23)$$

$$K_{CT}(\tilde{q}) = \frac{5}{6} g_v^{\pi\pi} \frac{\tilde{q}}{(1+\tilde{q})^2} - g_v^{\pi N} \frac{1}{1+\tilde{q}}. \quad (24)$$

The constant L_π is defined as $L_\pi = \ln \frac{\mu^2}{m_\pi^2}$, with μ being the renormalization scale. To estimate the correction of the transition operators at N2LO, following Ref.⁷⁵, we choose $\mu_{us} = m_\pi$ to eliminate all the terms depending on $\ln \frac{m_\pi^2}{\mu_{us}^2}$, and the LECs of the counterterms as $g_v^{\pi\pi} = -7.6 - (36/5) \ln(\mu/m_\rho)$ ⁷⁶, $g_v^{NN} = 0.614$ ⁷⁷ and $g_v^{\pi N} = 0$. For comparison, we also evaluate the correction with $g_v^{\pi\pi} = 0$. We find that the N2LO correction is generally less than 0.1 for a reasonable range of μ and its scale dependence becomes much weaker with the choice of nonzero $g_v^{\pi\pi}$ (Extended Data Table 1 and Extended Data Figure 3).

Acknowledgements

We thank J. de Vries, G. Li, C. F. Jiao, J. Menéndez, J. Meng, E. Mereghetti, and R. Wirth for fruitful discussions. We thank C. Forssén for providing the non-implausible interactions samples. This work is supported in part by the National Natural Science Foundation of China (Grant No. 12141501), the Guangdong Basic and Applied Basic Research Foundation (2023A1515010936), the U.S. Department of Energy, Office of Science, Office of Nuclear Physics under Awards No. DE-SC0023516, No. DE-SC0023175 (NUCLEI SciDAC-5 Collaboration), DE-FG02-97ER41014, DE-FG02-97ER41019, DE-AC02-06CH11357, and DE-SC0015376 (the DBD Topical Theory Collaboration), NSERC, the Arthur B. McDonald Canadian Astroparticle Physics Research Institute, the Canadian Institute for Nuclear Physics, the Deutsche Forschungsgemeinschaft (DFG, German Research Foundation) – Project-ID 279384907 – SFB 1245, and the European Research Council (ERC) under the European Union’s Horizon 2020 research and innovation programme (Grant Agreement No. 101020842). TRIUMF receives funding via a contribution through the National Research Council of Canada. A.M.R. acknowledges the support from NextGenerationEU/PRTR funding. The work of T.R.R. was funded by the Spanish MCIN under contracts PGC2018-094583-B-I00 and PID2021-127890NB-I00. The IM-GCM calculations were carried out using the computing resources provided by the Institute for Cyber-Enabled Research at Michigan State University, the GENCI-TGCC (Contract No. A0130513012) and CCRT HPC (TOPAZE su-

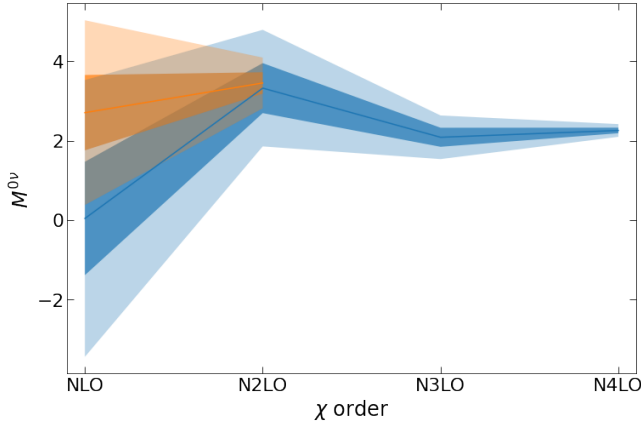
percomputer) at Bruyères-le-Châtel, and the U.S. National Energy Research Scientific Computing Center (NERSC), a DOE Office of Science User Facility supported by the Office of Science of the U.S. Department of Energy under Contract No. DE-AC02-05CH11231. The VS-IMSRG computations were performed with an allocation of computing resources on Cedar at WestGrid and Compute Canada, and on the Oak Cluster at TRIUMF managed by the University of British Columbia Department of Advanced Research Computing (ARC).

Author contributions statement

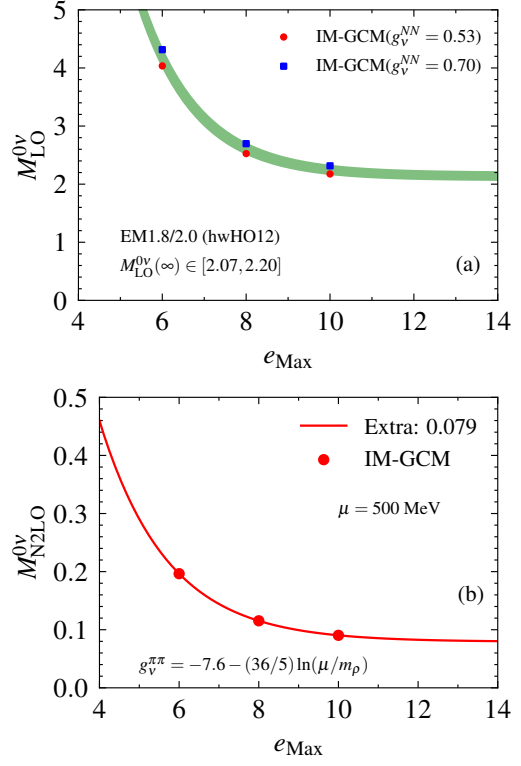
A.B., B.B., A.M.R., J.M.Y. performed the calculations. H.H., T.M., computed chiral forces for the IMSRG calculations. A.B. and J.P. developed the MM-DGP emulator. J.E., H.H., J.M.Y. are developers of IM-GCM and transition operators. H.H., J.H., R.S. are developers of VS-IMSRG, B.B., J.E., A.M.R. T.R., J.M.Y. and X.Z. implemented new algorithms for IM-GCM calculations. All authors discussed the results and contributed to the manuscript at all stages.

Author information

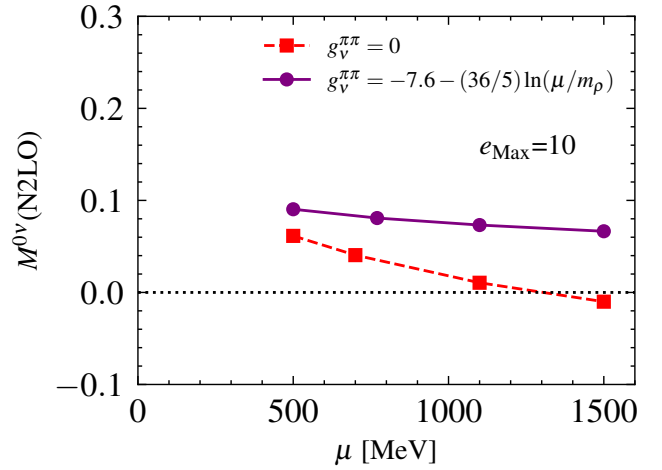
Reprints and permissions information is available at www.nature.com/reprints. The authors declare no competing financial interests. Readers are welcome to comment on the online version of the paper. Correspondence and requests for materials should be addressed to A.B. (abelley@triumf.ca) and J.M.Y. (yaojm8@susu.edu.cn).



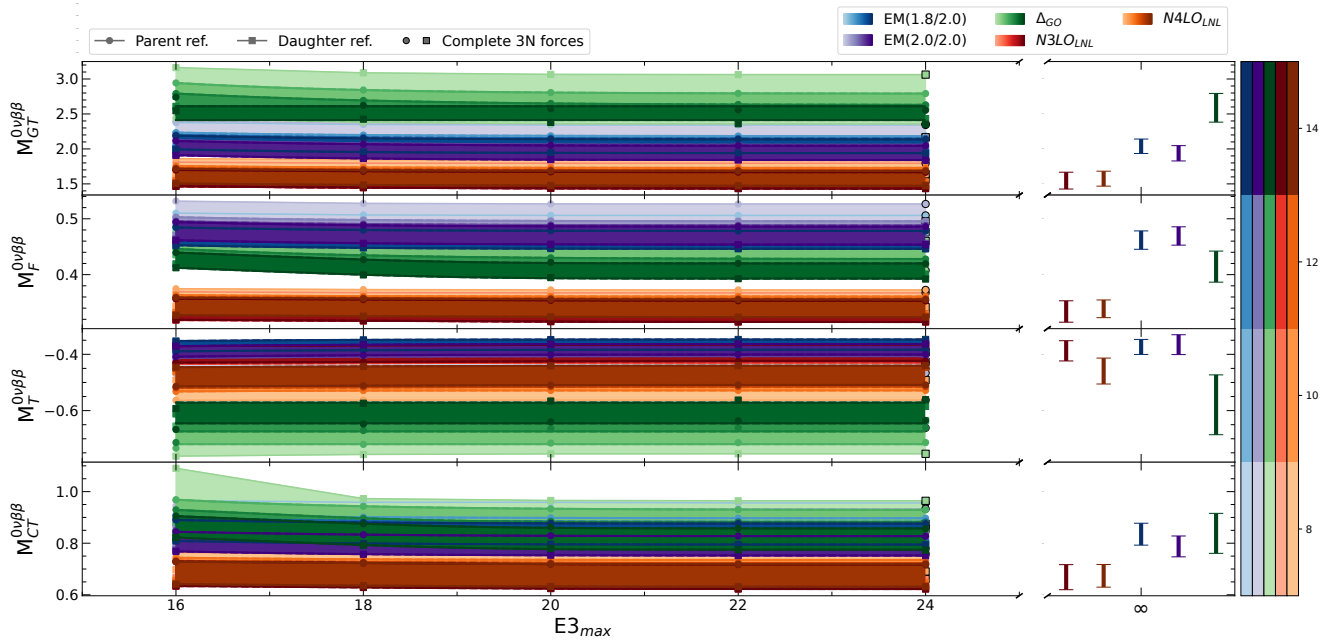
Extended Data Figure 1. Convergence of the NMEs of $0\nu\beta\beta$ decay for ^{76}Ge with respect to the truncation order of nuclear interactions in the chiral EFT. The results by the EMN chiral interactions^{37,38} (in blue) at NLO, N2LO, N3LO and N4LO are compared to those by the $\Delta_{\text{GO}}(394)$ ^{35,70} interactions (in orange) at NLO and N2LO upon which this work are based. The 68% (95%) degree of belief intervals computed following Ref.³⁶ are shown with the dark (light) bands. The NMEs are calculated with the VS-IMSRG at $e_{\text{Max}} = 10$. The use of the EMN interaction at NLO yield very small NMEs due to its poor reproduction of the 1S_0 phase shift.



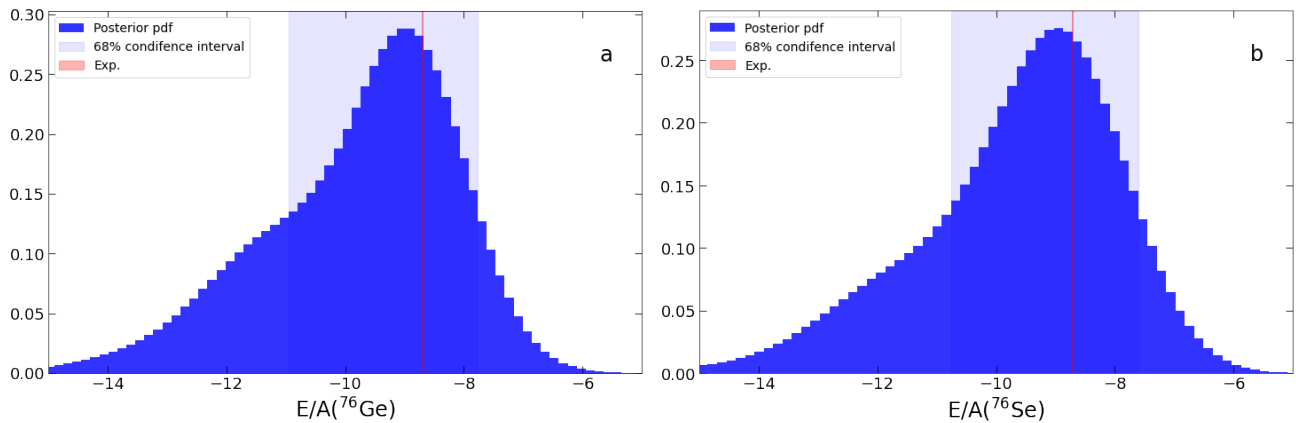
Extended Data Figure 2. Convergence of the NMEs of $0\nu\beta\beta$ decay for ^{76}Ge with respect to the e_{Max} . The results are given by the IM-GCM calculation using the EM1.8/2.0 chiral interaction⁸⁰ with frequency $\omega = 12$ MeV and transition operators truncated at the (a) LO and (b) N2LO. Two different values of the LEC for the SR contact transition operators are employed.



Extended Data Figure 3. The contribution of transition operators at N2LO to the NME as a function of the renormalization energy scale μ . Two different choices of $g_v^{\pi\pi}$, with the ultrasoft scale $\mu_{us} = m_\pi$, are employed. The results are given by the IM-GCM calculation using the EM1.8/2.0 chiral interaction⁸⁰ with frequency $\omega = 12$ MeV.



Extended Data Figure 4. Convergence of the NMEs with respect to both e_{\max} and $E_{3\max}$ for the five nuclear interactions from the VS-IMSRG calculation. Color gradient show increasing value of e_{\max} . The results at a fix value of e_{\max} are extrapolated to $E_{3\max} = 3e_{\max}$. The final NMEs are then extrapolated from the values containing all forces, giving $M^{0\nu\beta\beta} \in [2.10, 3.09]$.



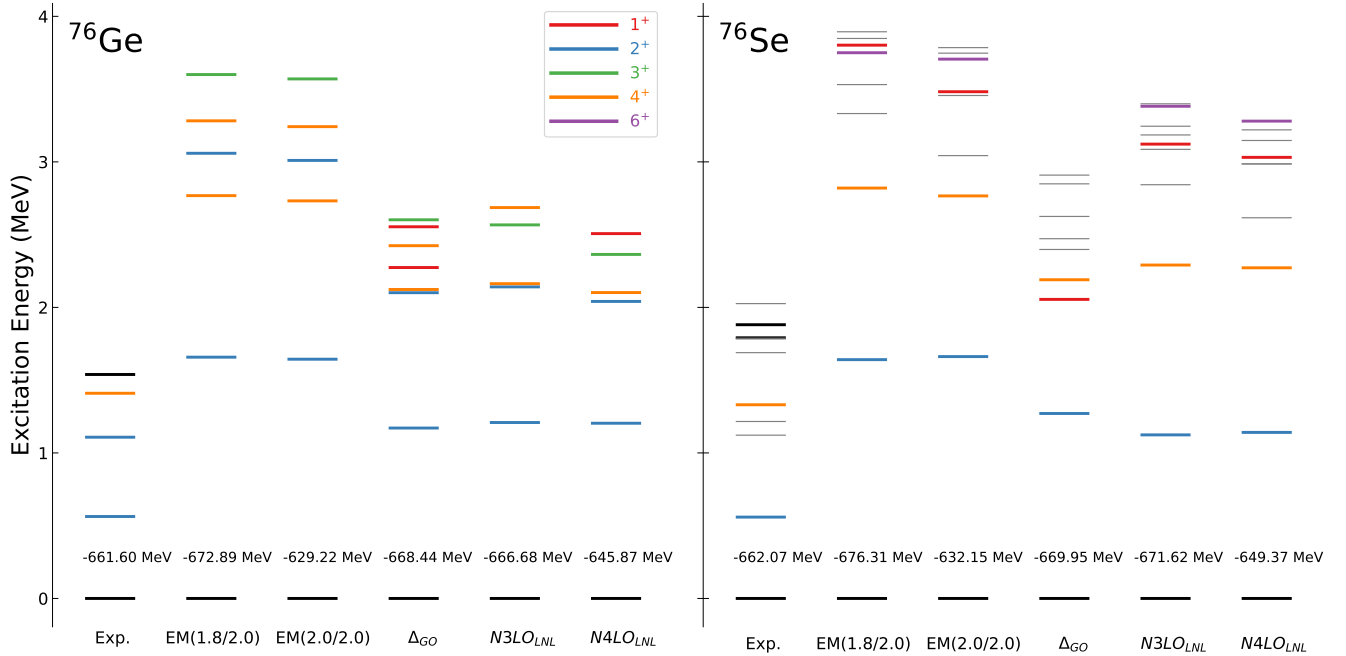
Extended Data Figure 5. Predictive distribution of the ground state energies (MeV) per nucleon in ^{76}Ge and ^{76}Se . The 1S_0 phase shift at 50 MeV are used as calibrating observables.

Extended Data Table 1. Decomposition of the NME $M^{0\nu}$ into different components for ^{76}Ge . The results are obtained from the IM-GCM calculations using the chiral interaction EM1.8/2.0 with frequency $\omega = 12$ MeV and different values of e_{Max} . The $M_{\text{LO,LR}}^{0\nu}(1,2,3)$ are for the NMEs by the leading-order long-range (LO,LR) transition operators corresponding to (1)-(3) of Fig. 1(a), and $M_{\text{LO,SR}}^{0\nu}$ by the short-range (LO,SR) operators corresponding to (6) of Fig. 1(a) with uncertainty originated from the LEC g_v^{NN77} . The NME $\tilde{M}_{\text{LO,LR}}^{0\nu}$ by the frequently employed long-range transition operators is composed of VV, AA, AP, PP and MM terms with parameterized dipole form factors and contains the LO and partial N2LO contributions, i.e., $\tilde{M}_{\text{LO,LR}}^{0\nu} = M_{\text{LO,LR}}^{0\nu}(1,2,3) + M_{\text{N2LO,LR}}^{0\nu}(4)$. With the promotion of the SR contact operator into LO, the NME at LO becomes $\tilde{M}_{\text{LO}}^{0\nu} = \tilde{M}_{\text{LO,LR}}^{0\nu} + M_{\text{LO,SR}}^{0\nu}$. The NME by the one-loop diagrams at N2LO is labeled with $M_{\text{N2LO}}^{0\nu}(5)$, where the renormalization scale $\mu = 500$ MeV and $\mu_{us} = m_\pi$ are employed.

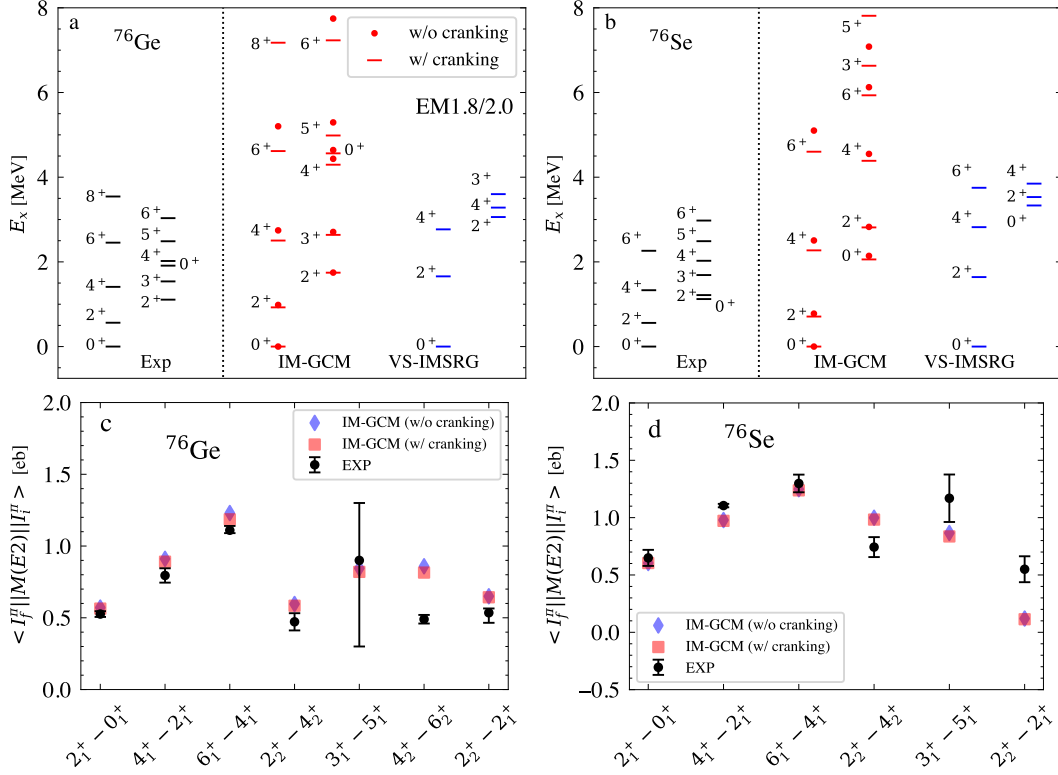
e_{Max}	$M_{\text{LO,LR}}^{0\nu}(1,2,3)$	$M_{\text{LO,SR}}^{0\nu}$	VV	GT-AA	GT-AP	GT-PP	GT-MM	T-AP	T-PP	T-MM	$\tilde{M}_{\text{LO,LR}}^{0\nu}$	$\tilde{M}_{\text{LO}}^{0\nu}$	$M_{\text{N2LO}}^{0\nu}(5)$
6	3.325	[0.872,1.152]	0.928	3.021	-0.900	0.285	0.227	-0.166	0.059	-0.024	3.170	[4.04, 4.32]	0.196
8	2.092	[0.533,0.704]	0.405	1.913	-0.549	0.173	0.138	-0.112	0.042	-0.018	2.020	[2.55, 2.72]	0.115
10	1.813	[0.437,0.577]	0.339	1.666	-0.460	0.142	0.113	-0.085	0.033	-0.015	1.744	[2.18, 2.32]	0.090
extrap	1.732	[0.399, 0.526]	0.329	1.596	-0.430	0.130	0.103	-0.058	0.023	-0.012	1.670	[2.07, 2.20]	0.079

Extended Data Table 2. The NMEs of double Gamow-Teller transition and $0\nu\beta\beta$ decay for ^{76}Ge . The results are obtained from the IM-GCM calculations with the EM chiral potentials in HO basis with frequency $\omega = 12$ MeV and different values of e_{Max} . The uncertainty in the $M_{\text{LO}}^{0\nu}$ is propagated from the uncertainty of the LEC g_v^{NN77} .

Interaction	M_{DGT}	$M_{\text{LO,LR}}^{0\nu}$	$M_{\text{LO,SR}}^{0\nu}/(-2g_v^{NN})$	$M_{\text{LO,SR}}^{0\nu}$	$M_{\text{LO}}^{0\nu}$
1.8/2.0($e_{\text{Max}} = 6$)	0.57	3.170	0.824	[0.872,1.152]	[4.042, 4.322]
1.8/2.0 ($e_{\text{Max}} = 8$)	0.42	2.020	0.503	[0.533,0.704]	[2.553, 2.724]
1.8/2.0($e_{\text{Max}} = 10$)	0.22	1.744	0.412	[0.437,0.577]	[2.181, 2.321]
1.8/2.0(extra.)	-	1.670	0.376	[0.399, 0.526]	[2.069, 2.197]
1.8/2.0 ($e_{\text{Max}} = 8$, cranking)	0.45	2.213	0.553	[0.585, 0.773]	[2.797, 2.986]
2.0/2.0 ($e_{\text{Max}} = 6$)	0.27	1.71	0.477	[0.505, 0.667]	[2.220, 2.382]
2.0/2.0 ($e_{\text{Max}} = 8$)	0.19	1.36	0.395	[0.418, 0.552]	[1.779, 1.913]



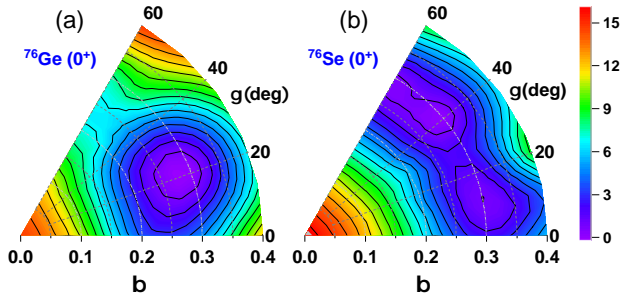
Extended Data Figure 6. Energy spectra of ^{76}Ge and ^{76}Se . The theoretical results are obtained from the VS-IMSRG calculations using the five nuclear chiral interactions.



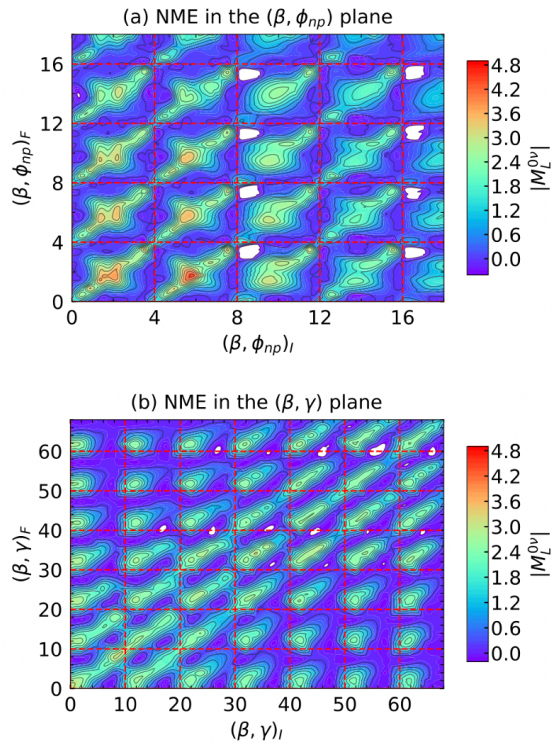
Extended Data Figure 7. The low-lying states of ^{76}Ge and ^{76}Se . **a, b**, The energy spectra of ^{76}Ge and ^{76}Se . **c, d**, The electric quadrupole transition matrix elements $\langle I_f^{\pi} || M(E2) || I_i^{\pi} \rangle$ of ^{76}Ge and ^{76}Se . The results from the VS-IMSRG are compared with those of IM-GCM calculation with and without the inclusion of cranking configurations. The data are taken from Refs. [41,42](#).

Extended Data Table 3. Structural properties of ^{76}Ge and ^{76}Se . The results are obtained from the IM-GCM calculations using the EM chiral interactions in HO basis with frequency $\omega = 12$ MeV and different values of e_{Max} . All energies are in MeV, and reduced E2 transition matrix element in eb. Uncertainties are originated from different choices of subspaces for the states.

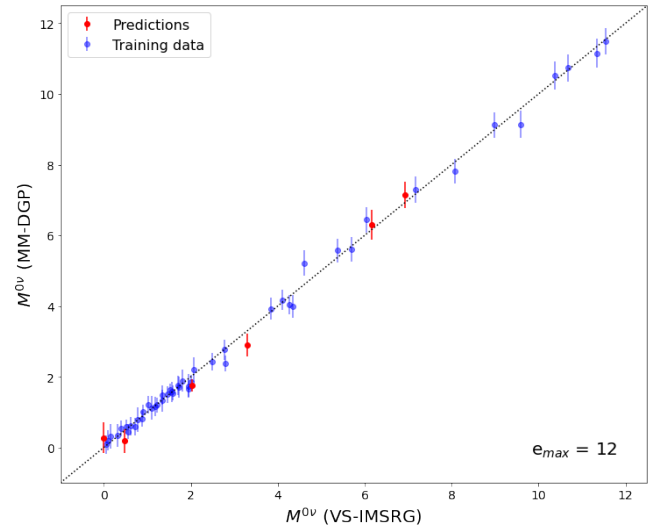
^{76}Ge	$EM\lambda/\Lambda(e_{\text{Max}})$	$E/A(0_1^+)$	$E_x(2_1^+)$	$E_x(4_1^+)$	$\langle 2_1^+ M(E2) 0_1^+ \rangle$	$\langle 2_1^+ M(E2) 2_1^+ \rangle$	$\langle 4_1^+ M(E2) 2_1^+ \rangle$
	EM2.0/2.0(6)	-6.751	0.81	2.04	0.55	-0.20	0.85
	EM2.0/2.0(8)	-7.522	0.85	2.43	0.48	-0.18	0.69
	EM1.8/2.0(6)	-7.879	1.05(14)	2.60(20)	0.48(2)	-0.40(5)	0.73(2)
	EM1.8/2.0(8)	-8.508	0.98	2.74	0.57	-0.22	0.91
	EM1.8/2.0(8, cranking)	-8.508	0.92	2.50	0.56	-0.21	0.89
	EM1.8/2.0(10)	-8.766	0.94(16)	2.55(56)	0.49(1)	-0.16(8)	0.63(1)
	Exp.	-8.705	0.563	1.41	0.526(2)	-0.24(2)	0.795(5)
^{76}Se	$EM\lambda/\Lambda(e_{\text{Max}}/\omega)$	$E/A(0_1^+)$	$E_x(2_1^+)$	$E_x(4_1^+)$	$\langle 2_1^+ M(E2) 0_1^+ \rangle$	$\langle 2_1^+ M(E2) 2_1^+ \rangle$	$\langle 4_1^+ M(E2) 2_1^+ \rangle$
	EM2.0/2.0(6)	-6.797	0.89	2.38	0.49	0.54	0.80
	EM2.0/2.0(8)	-8.498	0.89	2.62	0.53	0.61	0.76
	EM1.8/2.0(6)	-7.909	1.05(20)	2.80(25)	0.51(10)	0.41(4)	0.80(16)
	EM1.8/2.0(8)	-8.574	0.78	2.51	0.60	0.71	0.98
	EM1.8/2.0(8, cranking)	-8.574	0.70	2.27	0.60	0.70	0.97
	EM1.8/2.0(10)	-8.859	1.01(5)	2.54(23)	0.56(1)	0.69(1)	0.62(18)
	Exp.	-8.711	0.559	1.331	0.647(5)	-0.463 ⁺⁵² ₋₅₃	1.108 ⁺¹² ₋₁₁



Extended Data Figure 8. The energy surfaces of ^{76}Ge and ^{76}Se in the triaxial deformation parameters (β, γ) plane. The energies (normalized to the global minimum) of states are obtained from the calculation with projections onto the right particle numbers N, Z and angular momentum $I = 0$ using the IMSRG-evolved chiral interaction EM1.8/2.0. Neighboring contour lines are separated by 1.0 MeV.



Extended Data Figure 9. The configuration dependence of the NME for ^{76}Ge by the leading-order LR transition operators. In the panel (a), the NME changes as a function of the axial deformation parameter β and the neutron-proton isoscalar pairing amplitude ϕ_{np} of initial (I) and final (F) nuclei, where ϕ_{np} is a fixed to be 0, 4, 8, 12, and 16, respectively, while the value of β takes the value of $-0.4, -0.3, \dots, 0.3, 0.4$, respectively. In the panel (b), the NME changes as a function of the quadrupole deformation parameters (β, γ) , where γ is a fixed to be $0^\circ, 10^\circ, 20^\circ, 30^\circ, 40^\circ, 50^\circ$, and 60° , respectively, while the β takes the value of 0.1, 0.2, 0.3 and 0.4, respectively.



Extended Data Figure 10. Comparison of the emulated NMEs of the MM-DGP with the VS-IMSRG calculations. The NME of the VS-IMSRG are obtained with $e_{\text{Max}} = 12$ (the highest fidelity used for the emulator). Blue points are the training data and red points are predictions for test points. The root mean square error on the test points is 0.13.